

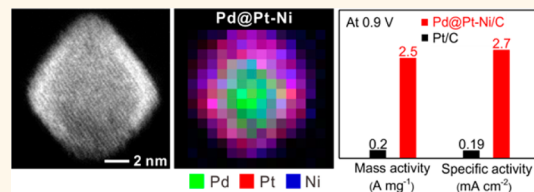
Synthesis and Characterization of Pd@Pt–Ni Core–Shell Octahedra with High Activity toward Oxygen Reduction

Sang-II Choi,[†] Minhua Shao,^{*,‡} Ning Lu,[§] Aleksey Ruditskiy,^{||} Hsin-Chieh Peng,^{||} Jinho Park,^{||} Sandra Guerrero,[#] Jinguo Wang,[§] Moon J. Kim,[§] and Younan Xia^{*,†,||,†,§}

[†]The Wallace H. Coulter Department of Biomedical Engineering, Georgia Institute of Technology and Emory University, Atlanta, Georgia 30332, United States,

[‡]Department of Chemical and Biomolecular Engineering, The Hong Kong University of Science and Technology, Clear Water Bay, Kowloon, Hong Kong, [§]Department of Materials Science and Engineering, University of Texas at Dallas, Richardson, Texas 75080, United States, ^{||}School of Chemistry and Biochemistry, Georgia Institute of Technology, Atlanta, Georgia 30332, United States, [#]UTC Power, South Windsor, Connecticut 06074, United States, and [†]School of Chemical and Biomolecular Engineering, Georgia Institute of Technology, Atlanta, Georgia 30332, United States. Contact Y. Xia for synthesis and characterization and M. Shao for electrochemical measurements and *in situ* XRD characterization.

ABSTRACT The oxygen reduction reaction (ORR) on the cathode of a polymer electrolyte fuel cell requires the use of a catalyst based on Pt, one of the most expensive metals on the earth. A number of strategies, including optimization of shape or facet, formation of alloys with other metals, and incorporation of a different metal into the core, have been investigated to enhance the activity of a Pt-based catalyst and thus reduce the loading of Pt. This article reports the synthesis and characterization of Pd@Pt–Ni core–shell octahedra with high activity toward ORR. The octahedra with an edge length of 8 nm were obtained by directly depositing thin, conformal shells of a Pt–Ni alloy on Pd octahedra of 6 nm in edge length. The key to the success of this synthesis is the use of an *amphiphilic* solvent to ensure good compatibility between the solvents typically used for the syntheses of Pd and Pt–Ni nanocrystals. The core–shell structure was confirmed by a number of techniques, including scanning transmission electron microscopy, energy-dispersive X-ray spectroscopy mapping, *in situ* X-ray diffraction under H₂ and He, and electrochemical measurements. Relative to the state-of-the-art Pt/C catalyst, the Pd@Pt–Ni/C catalyst showed mass and specific ORR activities enhanced by 12.5- and 14-fold, respectively. The formation of a core–shell structure helped increase the electroactive surface area in terms of Pt and thus the mass activity. During an accelerated durability test, the mass activity of the Pd@Pt–Ni/C catalyst only dropped by 1.7% after 10 000 cycles.



KEYWORDS: core–shell nanocrystal · oxygen reduction · platinum catalyst · polymer electrolyte fuel cell

Platinum-based catalysts are essential to the oxygen reduction reaction (ORR) at the cathodes of polymer electrolyte fuel cells (PEFCs).^{1–6} Owing to the low abundance and high cost of Pt, it is not difficult to understand why commercialization of the PEFC technology remains impractical even after several decades of research.^{1–6} A potential solution lies in the reduction of Pt loading by substantially enhancing the mass activity (per unit mass of Pt, A mg_{Pt}⁻¹) of a Pt-based catalyst toward ORR.^{7–32} The mass activity of a catalyst is a product of its specific activity (per unit active site, mA cm_{Pt}⁻²) and its electroactive surface area (ESA, per unit mass of Pt, m_{Pt}² g_{Pt}⁻¹). Therefore, the mass activity can be enhanced by increasing both the specific activity and the ESA. The most

effective strategy for increasing the specific activity is to tune the d-band center and surface structure of Pt by alloying it with another metal such as Fe, Co, or Ni^{7–9} and simultaneously controlling the shape of and thus the type of facet on the catalyst.^{10–23} It has been shown that downshifting the d-band center of Pt can reduce the oxygen binding energy (E_0) relative to that of pure Pt, thereby improving the specific activity.^{7–9} Stamenkovic and co-workers have shown that the relationship between the specific activity and the E_0 of various Pt-based alloys follows a volcano plot, with the highest activity being observed at a medium value for E_0 .⁷ Based on this information, the optimal E_0 , and thus the highest enhancement in specific activity, can be

* Address correspondence to younan.xia@bme.gatech.edu, kemshao@ust.hk.

Received for review July 7, 2014 and accepted September 23, 2014.

Published online September 23, 2014
10.1021/nn5036894

© 2014 American Chemical Society

achieved by alloying Pt with Ni to generate a Pt–Ni bimetallic catalyst.^{7,15}

The E_0 of Pt is also dependent on the surface structures of the low-index facets typically exposed on the surface of a Pt nanocrystal. It has been shown that the specific activity on the low-index, single-crystal Pt surfaces in aqueous HClO_4 solution increased in the order of $\text{Pt}(100) \ll \text{Pt}(111) \approx \text{Pt}(110)$.¹⁰ In the case of the Pt–Ni alloy, however, the specific activities of the low-index surfaces were found to take a different trend of $\text{Pt–Ni}(100) < \text{Pt–Ni}(110) \ll \text{Pt–Ni}(111)$.¹⁵ Since the E_0 and the specific activity of Pt are determined by both alloying Pt with a transition metal and the exposure of a specific facet, a number of groups have investigated shape-controlled syntheses of Pt–M (M = Fe, Co, and Ni) bimetallic nanocrystals.^{11–20} Inspired by the work from the Fang and Yang groups,^{11,16} we recently demonstrated that Pt–Ni octahedra could display a 51-fold improvement in specific activity, relative to the state-of-the-art Pt/C catalyst at 0.93 V, when the surface was covered by clean, well-stabilized {111} facets.¹²

The ESA in terms of Pt can be increased by coating Pt on a less-expensive core, thereby creating a core–shell structure.^{24–31} The resultant Pt loading of the core–shell structure is always lower than the same-sized nanoparticle made of pure Pt, resulting in a greater mass activity. Recently, palladium, about half of the price for Pt, has received much attention as a core material.^{24,27,29–31} Both theoretical and experimental studies have suggested that both the ESA and mass activity could be enhanced owing to the existence of a Pd core.^{24,26,27,31} As a good example, Pd–Pt core–shell dendrite nanocrystals have shown highly enhanced ESA and mass activity toward ORR when compared to those of a commercial Pt/C catalyst.^{24,31}

Taken together, the strategies for improving the mass activity of a Pt-based catalyst can be summarized as the follows: (i) incorporation of a transition metal such as Ni into the Pt lattice to form an alloy,^{11–16,20} (ii) optimization of the surface structure through shape-controlled synthesis,^{10–20} and (iii) construction of a core–shell structure by putting a metal less expensive than Pt in the core.^{24–31} Here we demonstrate the synthesis of an advanced catalyst for ORR that employs all of these strategies. The new catalyst is based on core–shell octahedra consisting of Pd in the core and a thin, conformal shell of Pt–Ni alloy enclosed by {111} facets, hereafter denoted as Pd@Pt–Ni octahedra. A major roadblock for the synthesis of such a core–shell structure is the compatibility between the solvents required for the syntheses of the Pd core and the Pt–Ni shell. In general, Pd nanocrystals with controlled shapes were synthesized in a hydrophilic solvent such as water, ethanol, or ethylene glycol (EG).³³ However, the synthesis of Pt–Ni bimetallic nanocrystals relied on the use of a hydrophobic solvent such as oleylamine

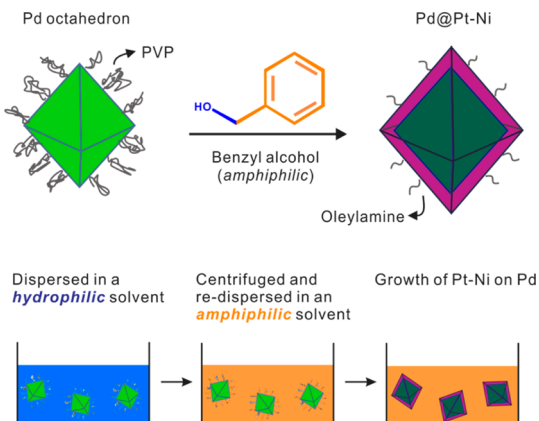


Figure 1. Schematic illustration of a procedure used to transfer the Pd nanocrystals from a hydrophilic solvent to an amphiphilic reaction medium and the preparation of Pd@Pt–Ni octahedra. The Pd octahedra were synthesized by reducing Na_2PdCl_4 in a hydrophilic medium containing PVP, ethanol, and water. Due to the amphiphilic property of benzyl alcohol, the PVP-capped Pd octahedra could be collected by centrifugation and then redispersed in benzyl alcohol. The Pd@Pt–Ni core–shell octahedra were obtained by heating a mixture of Pd octahedra, $\text{Pt}(\text{acac})_2$, $\text{Ni}(\text{acac})_2$, $\text{W}(\text{CO})_6$, oleylamine, and oleic acid in benzyl alcohol at 200 °C for 40 min.

(OAm), benzyl ether (BE), or dimethylfomamide (DMF)^{11–13,20} because Ni is subjected to quick oxidation in a hydrophilic solvent. As a result, the successful synthesis of Pd@Pt–Ni nanocrystals will need a solvent switching process, in which the Pd nanocrystals can be transferred from a hydrophilic solvent to a hydrophobic medium. Here we accomplished this goal by using an amphiphilic solvent such as benzyl alcohol (BA) for the formation of the Pt–Ni shell. The Pd@Pt–Ni/C catalyst showed a substantially increased ESA in terms of Pt, together with 12.5-fold enhancement in mass activity toward ORR when compared with the state-of-the-art Pt/C catalyst. This system also gives a much higher ORR mass activity than any other Pd–Pt core–shell nanostructures reported in the literature.^{24–31}

RESULTS AND DISCUSSION

Figure 1 illustrates the procedure used to transfer the Pd nanocrystals from a hydrophilic solvent to an amphiphilic reaction medium. Specifically, Pd octahedral seeds of 6 nm in edge length were prepared in a mixture of water and ethanol (a hydrophilic medium) by following our previously published protocol (Figure 2A).³³ Poly(vinylpyrrolidone) (PVP) was used as a colloidal stabilizer. The as-obtained Pd octahedra were collected by centrifugation and then redispersed in BA (an *amphiphilic* solvent). The overgrowth of Pt–Ni bimetallic shells on the Pd octahedral seeds was conducted in the presence of organic surfactants such as OAm and oleic acid (OAc). After the mixture of Pd octahedral seeds, $\text{Pt}(\text{acac})_2$, $\text{Ni}(\text{acac})_2$, $\text{W}(\text{CO})_6$, OAm, and OAc in BA had been heated at 200 °C for 40 min (see Experimental Section for details), we obtained

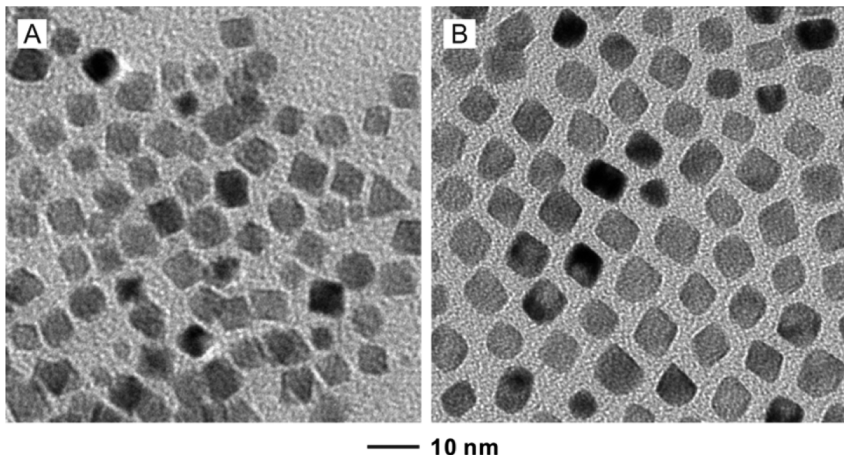


Figure 2. TEM images of (A) PVP-capped Pd octahedral seeds with an edge length of 6 nm and (B) Pd@Pt–Ni octahedra with an edge length of 8 nm (together with a shell thickness of 1 nm).

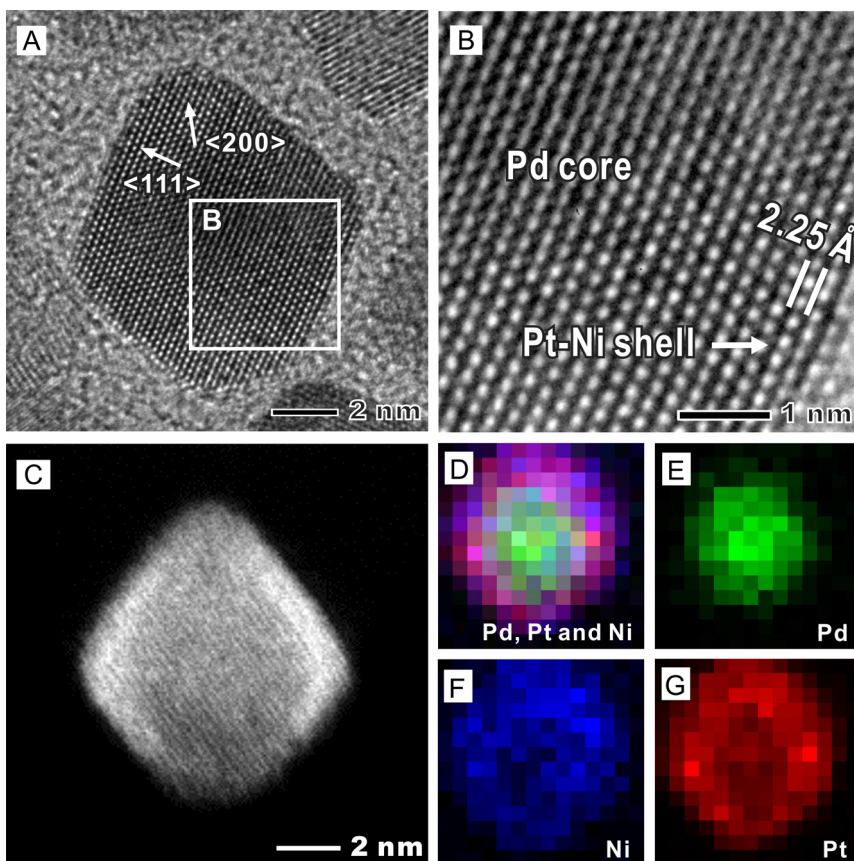


Figure 3. (A) High-resolution TEM image taken from a single Pd@Pt–Ni octahedron with an edge length of 8 nm. (B) High-resolution TEM image of the region marked by a box in (A). The lattice spacing of 2.25 Å for both the Pd core and the Pt–Ni shell confirms the epitaxial overgrowth of Pt–Ni on Pd. (C) HAADF-STEM image of a single Pd@Pt–Ni octahedron. The brighter shell on a relatively darker core indicates the difference in atomic number between Pt and Pd. (D–G) EDS mapping of elemental distributions for (D) Pd, Pt, and Ni, (E) Pt and Ni, (F) Pd and Ni, and (G) Pd and Pt.

Pd@Pt–Ni octahedra with an average edge length of 8 nm (Figure 2B). Supporting Information Figure S1 shows an additional transmission electron microscopy (TEM) image at a lower magnification to confirm the good uniformity in terms of size and shape for the Pd octahedral seeds and the Pd@Pt–Ni core–shell octahedral nanocrystals.

Figure 3A shows a high-resolution TEM image taken from a single Pd@Pt–Ni octahedron along the [011] zone axis, indicating a single-crystal structure with $\{111\}$ facets exposed on the side faces and $\{100\}$ facets at the truncated corners. The high-resolution TEM image in Figure 3B was recorded from the edge of the Pd@Pt–Ni octahedron boxed in Figure 3A.

It reveals the continuous lattice fringes between the Pd core and the Pt–Ni shell, which was about 1 nm thick. Based on X-ray diffraction (XRD), the *d*-spacing between the {111} planes of face-centered cubic (fcc) Pd is 2.25 Å (JCPDF #05-0681). As shown in our previous work by high-resolution TEM,¹² the lattice spacing between the {111} planes of Pt–Ni octahedra was 2.25(±0.05) Å. This negligible mismatch in lattice constants between Pd and Pt–Ni played a critical role in ensuring an epitaxial deposition of Pt–Ni on Pd.³⁴ The conventional XRD pattern for the Pd@Pt–Ni octahedra is shown in Supporting Information Figure S2. Previous study indicates that Pd@Pt nanocrystals would display asymmetric diffraction peaks because of the difference in lattice constant between Pd and Pt.²⁹ In the present work, the diffraction pattern of the Pt–Ni shell and the Pd core showed a single peak overlapped at the Pd(111) plane, showing nearly mirror symmetry due to the close matching in *d*-spacing between Pd and Pt–Ni. Figure 3C shows a high-angle annular dark-field scanning TEM (HAADF-STEM) image of a single Pd@Pt–Ni octahedron. The image reveals a brighter shell on a darker core, caused by the difference in atomic number between Pt and Pd. Energy-dispersive X-ray spectroscopy (EDS) mapping of the same region clearly shows pure Pd for the core and a Pt–Ni bimetallic composition for the shell (Figure 3D–G). Supporting Information Figure S3 shows a HAADF-STEM image of the same sample at a relatively lower magnification, confirming the formation of a core–shell structure in a large number of particles. After treatment with acetic acid (HAc) for 30 min,^{12,20,35,36} we used inductively coupled plasma-mass spectroscopy (ICP-MS) to measure the atomic ratios for the Pd@Pt–Ni octahedra. As shown in Table 1, the elemental ratios among Pd, Pt, and Ni were 1:1:0.55.

TABLE 1. Comparison of the Electrocatalytic Properties in Terms of ESA and ORR Specific (SA) and Mass Activities (MA) for the Pd@Pt–Ni/C and State-of-the-Art Pt/C Catalysts

catalysts	Pd/Pt/Ni atomic ratio	ESA _{Cu} (m ² g _{Pt} ⁻¹) ^a	SA _{Cu} (mA cm ⁻²) ^b	MA _{Pt} (A mg _{Pt} ⁻¹) ^b
Pt/C		106	0.19	0.2
Pd@Pt–Ni/C ^c	1:1:0.55	93	2.7	2.5

^a Measured from Cu_{UPD}. ^b Measured at 0.9 V (vs RHE). ^c Treated with HAc for 30 min.

The change in hydrophobicity between the solvents could affect the dispersion of Pd seeds and subsequent overgrowth of Pt–Ni onto their surfaces. As a result, we systematically evaluated a number of different combinations of solvents. When a hydrophilic solvent containing water was used for the synthesis, Ni_xO_y nanoparticles were found along with the Pd@Pt–Ni octahedra due to the easy oxidation of Ni into Ni_xO_y (Figure 4A). Clusters or islands of Pt–Ni were found to grow from the Pd core if a solvent less hydrophilic than

BA was used for the synthesis. For instance, Pt–Ni nanocrystals with poorly defined shapes were obtained in a mixture of BA and 1-octadecene (Figure 4B). When BE instead of BA was used as the solvent, the PVP-capped Pd seeds could not be dispersed well. Consequently, many small Pt–Ni particles containing no Pd seeds were obtained, as shown in Figure 4C. We have also tried to replace the surfactant mixture of OAm and OAc with PVP, a colloidal stabilizer commonly used in the syntheses of noble-metal nanocrystals. However, the final product was found to display a hollow structure, as shown in Figure 4D and the inset image at a higher magnification. These results indicate that the Pt(acac)₂ precursor could be quickly reduced by OAm at 200 °C to retard the galvanic replacement reaction between Pd and Pt(acac)₂.^{12,17,19} In contrast, PVP was unable to reduce the Pt(acac)₂ precursor and quickly passivate the surface of the Pd seed. As a result, there was galvanic replacement reaction between the Pd octahedral seeds and Pt(acac)₂ when OAm was replaced by PVP,³⁷ leading to the formation of nanostructures with hollow interiors.

To confirm the core–shell structure, we used *in situ* XRD in different gas environments to characterize the Pd@Pt–Ni octahedra. Since both Pd and Pt–Ni have an fcc structure with a similar lattice constant, they cannot be easily distinguished using the conventional XRD under ambient conditions (Supporting Information Figure S2). However, we could easily separate the Pd phase from Pt–Ni phase by taking advantage of the hydrogen absorption capability of Pd. Figure 5 shows the *in situ* XRD patterns taken from Pd@Pt–Ni octahedra under He and H₂ gases. The design of the cell was discussed in a previous publication³⁰ and is shown in Supporting Information Figure S4 (see details in Experimental Section). It is well-known that Pd is an excellent storage material for hydrogen.³⁰ Upon being fully charged with hydrogen, the *in situ* XRD peaks of Pd would shift to smaller angles due to the formation of palladium hydrides, as shown in Supporting Information Figure S5 for a control sample based on the commercial Pd/C catalyst. If the Pd core is covered by a complete shell of the Pt–Ni alloy, the diffraction peak position should not be changed when the gas environment around the sample is switched from He to H₂ because hydrogen cannot penetrate through a Pt-based lattice. As shown in Figure 5 for the Pd@Pt–Ni octahedra, the *in situ* XRD patterns showed no difference between the He and H₂ environments. Based on the data, two conclusions can be drawn: (i) the Pd core was completely covered by the Pt–Ni bimetallic shell so that no Pd was accessible to H₂; (ii) the Pt–Ni shell was sufficiently thick (around 1 nm, as estimated from the HAADF-STEM results) to prevent hydrogen from diffusing into the Pd core during the course of the diffraction experiment.

The core–shell structure was also supported by electrochemical measurements. Supporting Information

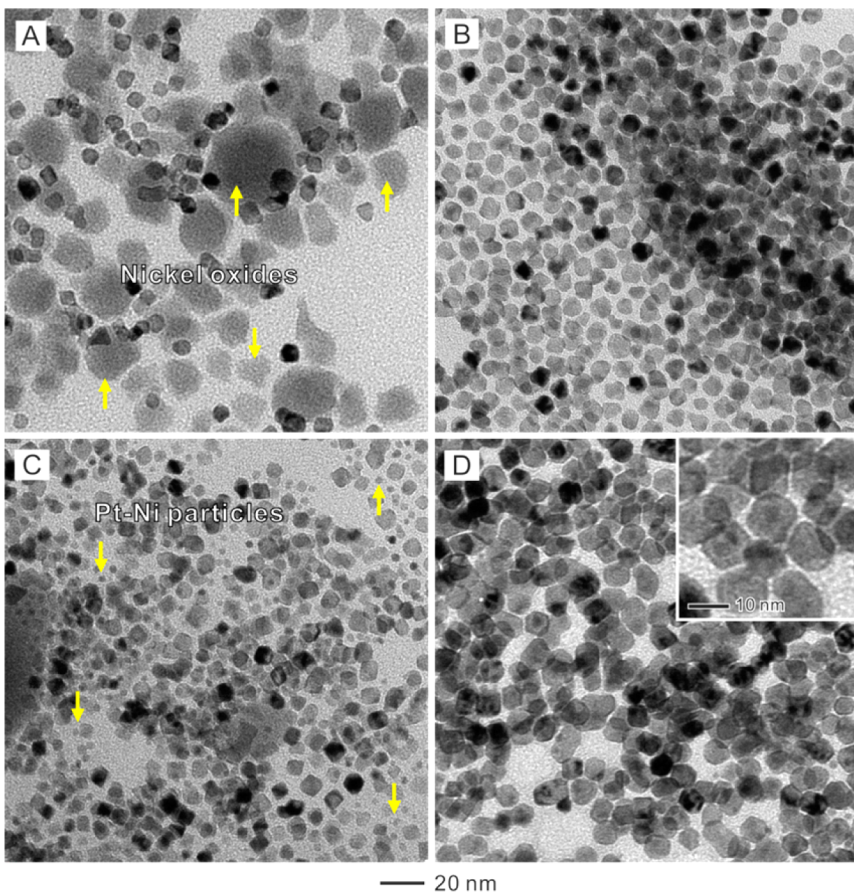


Figure 4. (A) TEM image of Pd@Pt–Ni nanocrystals (mixed with nickel oxides) synthesized in a mixture of benzyl alcohol, DI water, and ethanol. In this case, the Ni was easily oxidized to nickel oxides, as indicated by the arrows. (B) TEM image of Pd@Pt–Ni nanocrystals obtained in a mixture of benzyl alcohol and 1-octadecene. In this case, the Pt–Ni shell growing on the Pd seeds was observed to take an irregular shape. (C) TEM image of Pd@Pt–Ni nanocrystals synthesized in benzyl ether instead of benzyl alcohol. Since the PVP-capped Pd seeds were not dispersed well in a hydrophobic solvent, many small Pt–Ni particles (as indicated by the arrows) were formed through self-nucleation without involving Pd seeds. (D) TEM image of Pt-based nanocrystals with hollow structures obtained by using PVP, instead of a mixture of oleylamine and oleic acid, as the surfactant. The inset in (D) shows a TEM image at a higher magnification to clearly reveal both the hollow structure and the unreacted Pd cores in some particles.

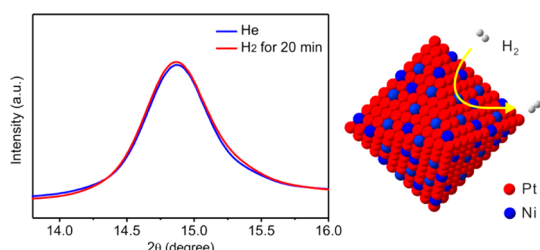


Figure 5. *In situ* XRD patterns taken from Pd@Pt–Ni core–shell nanocrystals under He (blue) and H₂ (red). Schematic drawing of the corresponding core–shell nanocrystal is shown on the right side.

Figure S6 shows a cyclic voltammogram (CV) of the HAc-treated Pd@Pt–Ni octahedra deposited on a carbon support (Pd@Pt–Ni/C catalyst, Figure S7A) in a N₂-saturated, 0.1 M HClO₄ solution. The CVs in the hydrogen desorption region are compared in Figure 6A for the Pd (blue line) and Pd@Pt–Ni octahedra (red line). After the deposition of a Pt–Ni shell, the sharp peak at

0.29 V (vs reversible hydrogen electrode, RHE) associated with the desorption of hydrogen from the Pd surface disappeared,³⁸ while the desorption of hydrogen shifted to more negative potentials. The large difference in the region of hydrogen desorption confirms changes to the surface properties upon the formation of a Pt–Ni shell on the Pd core as revealed by *in situ* XRD measurement. Furthermore, the features of hydrogen desorption on the Pd@Pt–Ni/C catalyst are very similar to those on the octahedral Pt–Ni/C catalyst reported previously.^{12,38} The uniform deposition of a Pt–Ni bimetallic shell on the Pd core is also confirmed by the CO stripping results, as shown in Figure 6B. The main CO stripping peak for octahedral Pd/C was located at 1.0 V (blue line). For the Pd@Pt–Ni/C catalyst, the peak was shifted to 0.76 V, which is again very close to the position reported for the octahedral Pt–Ni/C catalyst.^{12,38–40} These results indicate the formation of a complete shell of Pt–Ni on the Pd core, which is consistent with the HAADF-STEM, EDS, and *in situ* XRD data.

To evaluate the electronic structure of the Pd@Pt–Ni octahedra, we performed X-ray photoelectron spectroscopy (XPS) measurements (Figure 7). The black and red traces correspond to the as-obtained and

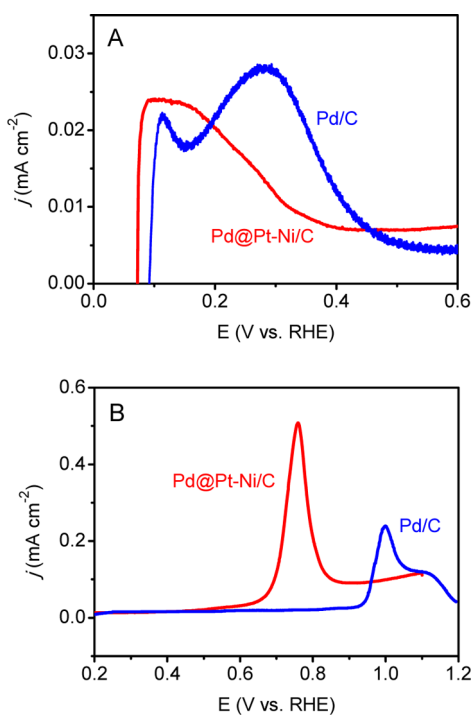


Figure 6. (A) CV curves in the hydrogen desorption region and (B) CO stripping curves for Pd/C (blue line, octahedral shape) and Pd@Pt–Ni/C (red line) catalysts. Scanning rate = 50 mV s⁻¹.

HAc-treated nanocrystals, respectively. Since the other metal in a Pt-based alloy could modify the electronic structure of Pt, the binding energy of Pt 4f XPS peaks in the Pd@Pt–Ni octahedra was increased by 0.5 eV relative to that of pure Pt (Figure 7A).^{3–9} Similar to the Pt 4f, the Pd 3d XPS peaks were shifted to higher binding energy positions (Figure 7B). In addition, we can determine the surface cleanliness and the effect of HAc treatment from the XPS analysis. Figure 7C indicates that the N 1s peak (398 eV) from OAm was barely observed from the as-obtained Pd@Pt–Ni core–shell octahedra and no signal was detected for the HAc-treated samples. As indicated in our previous work, introducing a proper solvent could reduce the coverage of surfactants such as OAm and OAc on the Pt surface.¹² In this system, we believe that BA could reduce the coverage of both OAm and OAc while achieving an octahedral shape for the core–shell nanocrystals. Figure 7D shows the Ni 2p spectra of samples before and after HAc treatments. The Ni 2p spectrum of the as-obtained Pd@Pt–Ni octahedra showed peaks of both Ni metal and Ni(OH)₂.^{39,41} After HAc treatment for 30 min, the peaks for Ni(OH)₂, as well as their satellites, disappeared. Only those peaks associated with Ni remained.

Finally, we compared the ORR activity of the Pd@Pt–Ni/C catalyst with the state-of-the-art Pt/C catalyst (TEC10E50E, TKK, 2.5 nm) using the thin film rotating disk electrode (RDE) technique in an O₂-saturated, 0.1 M HClO₄ solution at room temperature (Figure 8A). The ESA of the Pd@Pt–Ni/C catalyst

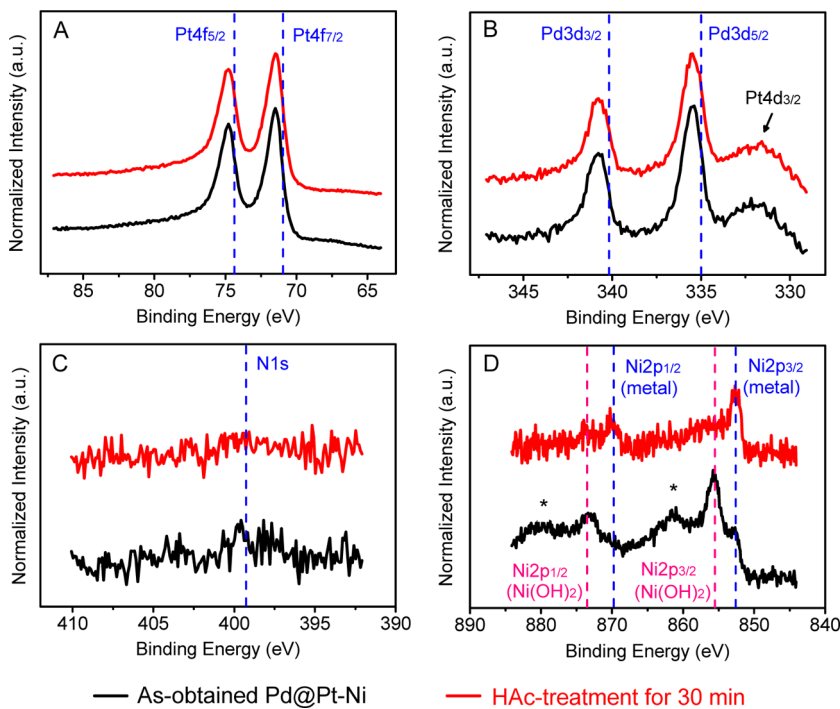


Figure 7. XPS spectra of the as-synthesized and HAc-treated Pd@Pt–Ni core–shell octahedra: (A) Pt 4f, (B) Pd 3d, (C) N 1s, and (D) Ni 2p. The asterisks (*) in (D) indicate satellite peaks of the corresponding Ni 2p peaks for Ni(OH)₂.

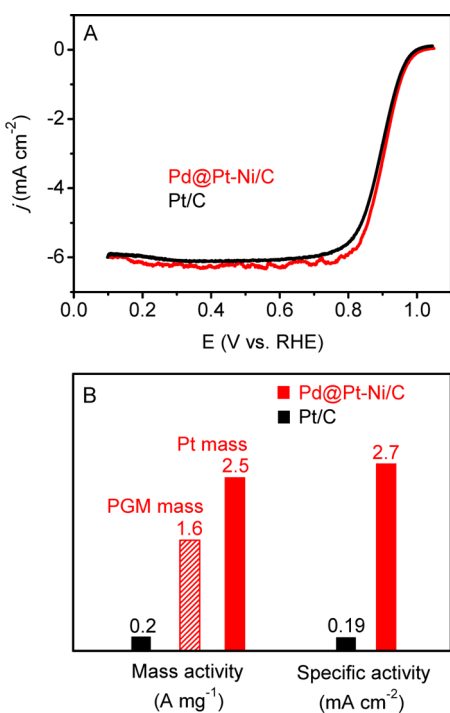


Figure 8. (A) Comparison of positive-going ORR polarization curves for the Pd@Pt–Ni/C and state-of-the-art Pt/C (TKK) catalysts in an O₂-saturated, 0.1 M aqueous HClO₄ solution. Scanning rate = 10 mV s⁻¹. Rotation speed = 1600 rpm. The currents were normalized to the geometric area of the rotating disk electrode (0.196 cm²). The Pt loadings on the electrodes were 0.65 and 4.0 μ g, respectively, for the Pd@Pt–Ni/C and Pt/C catalysts. (B) Comparison of mass (in terms of Pt and platinum group metal, PGM) and specific ORR activities for the Pd@Pt–Ni/C and state-of-the-art Pt/C (TKK) catalysts at 0.9 V.

was 93 m² g_{Pt}⁻¹, similar to that of Pt/C catalyst (106 m² g_{Pt}⁻¹) calculated from the charges for Cu underpotential deposition (Cu_{UPD}, Figure S8 and Table 1), even though the edge length of the Pd@Pt–Ni octahedra was three times the particle size of the Pt/C catalyst. The ORR polarization curve of the Pd@Pt–Ni/C catalyst was 15 mV more positive than Pt/C even though the Pt loading of the former on the RDE was much lower (0.65 vs 4.0 μ g). The mass activity of the Pd@Pt–Ni/C catalyst was 2.5 A mg_{Pt}⁻¹ at 0.9 V, which was 12.5 times higher than that of the Pt/C catalyst (Figure 8B and Table 1). The enhancement in mass activity also benefits from the improvement in specific activity (2.7 vs 0.19 mA cm⁻² for the Pd@Pt–Ni/C and Pt/C catalysts, respectively, Table 1), in good agreement with the prior observation of a significantly enhanced specific ORR activity on the {111} facet of Pt₃Ni single-crystal substrates relative to Pt/C.¹⁵ Based on the metal loadings

in the Pd@Pt–Ni/C catalyst (16 and 8.9 wt % for Pt and Pd, respectively), the total platinum group metal (PGM) mass activity was 1.6 A mg⁻¹ (Figure 8B). This value is much higher than any other Pt-based catalysts with a core–shell structure reported in the literature.^{24–30}

We also evaluated the stability of the Pd@Pt–Ni/C catalyst for ORR through an accelerated durability test by applying a linear potential sweep between 0.6 and 1.1 at 0.1 V/s in an O₂-saturated, 0.1 M HClO₄ solution at room temperature. After 10 000 cycles, the octahedral shape of the Pd@Pt–Ni nanocrystals was still retained with well-defined {111} facets, albeit some of them were slightly truncated at vertices (Supporting Information Figure S7B). In addition, a small portion of the Pd@Pt–Ni nanocrystals was shown to have a hollow structure due to the dissolution of the Pd cores. As shown in Figure S9, the ESA and mass activity of the Pd@Pt–Ni/C catalyst only dropped by 5.4 and 1.7%, respectively. When the data reported in literature for Pt–Ni octahedra are compared,^{12,14} it is clear that the durability of the Pd@Pt–Ni core–shell nanocrystals was greatly improved.²⁷ This enhancement in durability could be attributed to a favorable change to the Pt/Ni ratio during the test. We measured the amounts of Pt and Ni leached into the electrolyte by ICP-MS after the test and then determined the Pt/Ni ratio of Pd@Pt–Ni/C. After the durability test, the Pt/Ni ratio was increased from 1.8 to 2.1, placing it closer to the optimal value for the highest ORR activity, as defined by the volcano plot.²⁰ A systematic investigation of the stability under various conditions, including the potential used for cycling and thermal treatment, is underway and will be reported separately.

CONCLUSION

We have demonstrated the synthesis of an advanced ORR catalyst based on Pd@Pt–Ni octahedra by effectively combining three different strategies that involved alloying, shape control, and the formation a core–shell structure. After HAc treatment, the Pd@Pt–Ni/C catalyst showed an ORR mass activity of 12.5-fold higher and a specific activity of 14-fold greater than that of the state-of-the-art Pt/C catalyst. In addition, the mass activity of the Pd@Pt–Ni/C catalyst is also much higher than any of the Pt-based catalyst with a core–shell structure published in the literature. This work offers a general strategy for the design and synthesis of cost-effective catalysts based on Pt for ORR and thus large-scale commercialization of the PEFC technology.

EXPERIMENTAL SECTION

Materials. PVP (MW \approx 55 000), citric acid, sodium tetrachloropalladate(II) (Na₂PdCl₄), platinum(II) acetylacetone (Pt(acac)₂, 99.99%), nickel(II) acetylacetone (Ni(acac)₂, 95%), OAm (70%), OAc (90%), tungsten hexacarbonyl (W(CO)₆, 99.99%),

and BA (99.8%) were all obtained from Sigma-Aldrich. The chemicals were used as received.

Synthesis of Pd Octahedral Seeds. In a typical synthesis of Pd octahedral seeds, PVP (105 mg), citric acid (180 mg), and Na₂PdCl₄ (57 mg) were dissolved in a mixture of 3 mL of ethanol and 8 mL of water. The resulting solution was heated at 80 °C in

air under magnetic stirring for 3 h and cooled to room temperature. The final product was dispersed in BA after washing with DI water three times.³³

Synthesis of Pd@Pt–Ni Octahedra. In a typical synthesis, a mixture of Pt(acac)₂ (20 mg, 0.051 mmol), Ni(acac)₂ (10 mg, 0.039 mmol), OAm (2.0 mL), and OAc (1.0 mL) was added into BA (7.0 mL) including the Pd octahedral seeds (corresponding to 0.051 mmol of Na₂PdCl₄ precursor) and heated to 130 °C under an argon atmosphere with magnetic stirring. W(CO)₆ (50 mg, 0.142 mmol) was added quickly at 130 °C, and at the same time, argon purging was stopped. The mixture was then heated to 200 °C for 10 min at a heating rate of 10 °C min⁻¹ and kept at 200 °C for 40 min. The reaction mixture was cooled to room temperature naturally, and the Pd@Pt–Ni core–shell octahedra were precipitated out by sequentially adding toluene (5 mL) and ethanol (15 mL). The supernatant was removed by centrifugation at 6000 rpm for 10 min. The resulting Pd@Pt–Ni core–shell octahedra could be easily dispersed in an organic solvent such as toluene or hexane.

Preparation of the Pd@Pt–Ni/C Catalysts. A suspension of the Pd@Pt–Ni octahedra in toluene was mixed with Ketjen black carbon (~25 wt % of Pt) dispersed in toluene under ultrasonication for 10 min. The mixture was then stirred magnetically and ultrasonicated for another 3 h. The resulting Pd@Pt–Ni/C catalyst was centrifuged at 12 000 rpm for 15 min and added into 20 mL of acetic acid and heated at 60 °C for 30 min to clean the residual surfactants. The final catalyst was washed three times with ethanol and dried in an oven for 30 min before ORR measurements (Supporting Information Figure S7A).

Morphological, Structural, and Elemental Characterizations. TEM images were taken using a Hitachi-HT7700 microscope (Hitachi, Tokyo, Japan) operated at 120 kV by drop-casting the nanoparticle dispersions on carbon-coated copper grids and drying under ambient conditions. High-resolution TEM, HAADF-STEM, and EDS mapping analyses were all performed at 200 kV using a JEOL ARM200F microscope (JEOL, Tokyo, Japan) with STEM aberration corrector. Elemental compositions of the nanostructures were determined using NEXION 300Q ICP-MS (PerkinElmer, Waltham, MA). Conventional XRD pattern was recorded using a X'Pert PRO Alpha-1 diffractometer (PANalytical, Almelo, The Netherlands) with a 1.8 kW ceramic copper tube source.

In situ XRD experiments were performed at Beamline X18A at the National Synchrotron Light Source (NSLS) at the Brookhaven National Laboratory (BNL) in Upton, NY. A detailed experiment procedure can be found elsewhere.³⁰ Briefly, helium (99.999%, Praxair) and hydrogen (99.999%, Praxair) were gauged through the custom-made sample cell (Supporting Information Figure S4) by two mass flow controllers (Brooks 5850) with a flow rate of ~20 mL min⁻¹. The sample was first purged by He to prevent the catalyst powders from burning due to the combustion of H₂. The XRD spectra were recorded with a 2D detector (XRD 1621 N ES, PerkinElmer) at 20 keV (calibrated by the Mo K absorption edge) and subsequently analyzed using standard data processing software. The dark current was collected over 40 s (10 exposures at 4 s per exposure), and the diffraction pattern was recorded over 400 s (100 exposures at 4 s per exposure). *In situ* XRD patterns presented in this paper have been transformed to correspond to Cu K α incident radiation. After the XRD pattern under an inert atmosphere was recorded, the cell was purged with H₂ for 20 min and a new XRD pattern was then recorded under this atmosphere. Further purging with H₂ did not affect the structure of the material. Finally, the cell was purged with He for 10 min, and a post-H₂-exposure XRD pattern was recorded.

The sample to detector distance was approximately 400 mm and was calibrated by the use of titanium dioxide (rutile) powder loaded into the sample holder of the cell in a setting identical to what was used for catalyst characterization. Calculation of error propagation suggests that an error in sample position of ± 1 mm would result in an error in the lattice constant of ± 0.001 nm. While there is a possibility of sample misalignment, it was prevented through careful design. Further, there was an internal calibration standard for each sample in the form of amorphous carbon, whose peak is present in all of the

in situ XRD patterns collected in this work, and it was always positioned at the same 2 θ value.

Electrochemical Measurements. Approximately 3 mg of the catalyst was dispersed in a solvent consisting of 3 mL of water, 3 mL of isopropyl alcohol, and 15 μ L of 5% Nafion (Aldrich) by sonication for 10 min. Ten microliters of the suspension was deposited on a precleaned glassy carbon RDE (Pine Instruments) and allowed to dry in air. The electrode was cycled between 0.07 and 1.0 V at 100 mV s⁻¹ for 20 cycles in a N₂-saturated, 0.1 M HClO₄ solution until a stable CV curve was obtained. Then, CVs of H_{UPD} were recorded in a same condition at a scan rate of 50 mV s⁻¹. CVs of Cu_{UPD} were recorded for commercial Pt/C and Pd@Pt–Ni/C in a N₂-saturated solution containing 0.05 M H₂SO₄ and 0.05 M CuSO₄ at 5 mV s⁻¹. The charges associated with Cu_{UPD} were used to calculate the ESAs of all the samples, assuming 480 μ C cm⁻² for a full coverage of Cu_{UPD} on {111} facets. For CO stripping experiments, CO was adsorbed on the electrodes by holding the potential at 0.07 V for 10 min in a CO-saturated, 0.1 M HClO₄ solution. The CO stripping curve was recorded after the extra CO in solution was removed by purging N₂ for 30 min.

Oxygen reduction polarization curves were measured in an O₂-saturated, 0.1 M HClO₄ solution at a scan rate of 10 mV s⁻¹ and a RDE rotation speed of 1600 rpm. The kinetic current, j_k , at 0.9 V was derived from the Koutecky–Levich equation:

$$\frac{1}{j} = \frac{1}{j_k} + \frac{1}{B\omega^{1/2}}$$

where j is the measured current density, B is a constant, and ω is the rotation speed.

All the electrochemical measurements were conducted on a CHI730C (CH Instruments, Austin, TX) or PAR 273A (Princeton Applied Research, Trenton, NJ) potentiostat. A leak-free Ag/AgCl electrode was used as the reference electrode in the Cu_{UPD} and CO stripping experiments. A RHE was used for the ORR activity measurements. All potentials are presented relative to RHE. Pt gauze was used as a counter electrode in all of the electrochemical measurements.

Conflict of Interest: The authors declare no competing financial interest.

Acknowledgment. This work was supported in part by a research grant from UTC Power and startup funds from the Georgia Institute of Technology. Use of the National Synchrotron Light Source (NSLS) at Brookhaven National Laboratory was supported by the U.S. Department of Energy, Office of Science, Office of Basic Energy Sciences, under Contract No. DE-AC02-98CH10886. Beamlines X18A at the NSLS are supported in part by the Synchrotron Catalysis Consortium (DOE BES Grant DE-FG02-03ER15688).

Supporting Information Available: TEM images, conventional XRD data, the design of a sample cell for *in situ* XRD measurement, and CV and Cu_{UPD} curves of Pd@Pt–Ni/C catalyst. This material is available free of charge via the Internet at <http://pubs.acs.org>.

REFERENCES AND NOTES

- Ertl, G. *Handbook of Heterogeneous Catalysis*; Wiley-VCH: Weinheim, Germany, 2008.
- Department of Energy. Fuel Cell Technical Team Roadmap: Table 5. *Technical Targets for Electrocatalysts*, 2013; <http://www.eere.energy.gov>.
- Chen, A.; Holt-Hindle, P. Platinum-Based Nanostructured Materials: Synthesis, Properties, and Applications. *Chem. Rev.* **2010**, *110*, 3767–3804.
- Steele, B. C. H.; Heinzel, A. Materials for Fuel-Cell Technologies. *Nature* **2001**, *414*, 345–352.
- Vielstich, W.; Lamm, A.; Gasteiger, H. A. *Handbook of Fuel Cells: Fundamentals, Technology and Applications*; John Wiley & Sons: Chichester, U.K., 2003.
- Shao, M. *Electrocatalysis in Fuel Cells: A Non- and Low-Platinum Approach*; Springer: London, 2013.

7. Stamenkovic, V. R.; Mun, B. S.; Mayrhofer, K. J. J.; Ross, P. N.; Markovic, N. M.; Rossmeisl, J.; Greeley, J.; Nørskov, J. K. Changing the Activity of Electrocatalysts for Oxygen Reduction by Tuning the Surface Electronic Structure. *Angew. Chem., Int. Ed.* **2006**, *45*, 2897–2901.
8. Stamenkovic, V. R.; Mun, B. S.; Arenz, M.; Mayrhofer, K. J. J.; Lucas, C. A.; Wang, G.; Ross, P. N.; Markovic, N. M. Trends in Electrocatalysis on Extended and Nanoscale Pt-Bimetallic Alloy Surfaces. *Nat. Mater.* **2007**, *6*, 241–247.
9. Greeley, J.; Stephens, I. E. L.; Bondarenko, A. S.; Johansson, T. P.; Hansen, H. A.; Jaramillo, T. F.; Rossmeisl, J.; Chorkendorff, I.; Nørskov, J. K. Alloys of Platinum and Early Transition Metals as Oxygen Reduction Electrocatalysts. *Nat. Chem.* **2009**, *1*, 552–556.
10. Markovic, N. M.; Ross, P. N. Surface Science Studies of Model Fuel Cell Electrocatalysts. *Surf. Sci. Rep.* **2002**, *45*, 117–229.
11. Zhang, J.; Yang, H.; Fang, J.; Zou, S. Synthesis and Oxygen Reduction Activity of Shape-Controlled Pt_3Ni Nanopolyhedra. *Nano Lett.* **2010**, *10*, 638–644.
12. Choi, S.-I.; Xie, S.; Shao, M.; Odell, J. H.; Lu, N.; Peng, H.-C.; Protsailo, L.; Guerrero, S.; Park, J.; Xia, X.; Wang, J.; Kim, M. J.; Xia, Y. Synthesis and Characterization of 9-nm Pt–Ni Octahedra with a Record High Activity of $3.3 \text{ A/mg}_{\text{Pt}}$ for the Oxygen Reduction Reaction. *Nano Lett.* **2013**, *13*, 3420–3425.
13. Cui, C.; Gan, L.; Li, H.-H.; Yu, S.-H.; Heggen, M.; Strasser, P. Octahedral PtNi Nanoparticle Catalysts: Exceptional Oxygen Reduction Activity by Tuning the Alloy Particle Surface Composition. *Nano Lett.* **2012**, *12*, 5885–5889.
14. Cui, C.; Gan, L.; Heggen, M.; Rudi, S.; Strasser, P. Compositional Segregation in Shaped Pt Alloy Nanoparticles and Their Structural Behaviour during Electrocatalysis. *Nat. Mater.* **2013**, *12*, 765–771.
15. Stamenkovic, V. R.; Fowler, B.; Mun, B. S.; Wang, G.; Ross, P. N.; Lucas, C. A.; Markovic, N. M. Improved Oxygen Reduction Activity on $\text{Pt}_3\text{Ni}(111)$ via Increased Surface Site Availability. *Science* **2007**, *315*, 493–497.
16. Wu, J.; Gross, A.; Yang, H. Shape and Composition-Controlled Platinum Alloy Nanocrystals Using Carbon Monoxide as Reducing Agent. *Nano Lett.* **2011**, *11*, 798–802.
17. Choi, S.-I.; Choi, R.; Han, S. W.; Park, J. T. Shape-Controlled Synthesis of Pt_2Co Nanocrystals with High Electrocatalytic Activity toward Oxygen Reduction. *Chem.—Eur. J.* **2011**, *17*, 12280–12284.
18. Chen, C.; Kang, Y.; Huo, Z.; Zhu, Z.; Huang, W.; Xin, H. L.; Snyder, J. D.; Li, D.; Herron, J. A.; Mavrikakis, M.; Chi, M.; More, K. L.; Li, Y.; Markovic, N. M.; Somorjai, G. A.; Yang, P.; Stamenkovic, V. R. Highly Crystalline Multimetallic Nano-frames with Three-Dimensional Electrocatalytic Surfaces. *Science* **2014**, *343*, 1339–1343.
19. Kang, Y.; Murray, C. B. Synthesis and Electrocatalytic Properties of Cubic Mn–Pt Nanocrystals (Nanocubes). *J. Am. Chem. Soc.* **2010**, *132*, 7568–7569.
20. Choi, S.-I.; Xie, S.; Shao, M.; Lu, N.; Guerrero, S.; Odell, J. H.; Park, J.; Wang, J.; Kim, M. J.; Xia, Y. Controlling the Size and Composition of Nanosized Pt–Ni Octahedra To Optimize Their Catalytic Activities toward the Oxygen Reduction Reaction. *ChemSusChem* **2014**, *7*, 1476–1483.
21. Mayrhofer, K. J. J.; Blizanac, B. B.; Arenz, M.; Stamenkovic, V. R.; Ross, P. N.; Markovic, N. M. The Impact of Geometric and Surface Electronic Properties of Pt-Catalysts on the Particle Size Effect in Electrocatalysis. *J. Phys. Chem. B* **2005**, *109*, 14433–14440.
22. Shao, M.; Peles, A.; Shoemaker, K. Electrocatalysis on Platinum Nanoparticles: Particle Size Effect on Oxygen Reduction Reaction Activity. *Nano Lett.* **2011**, *11*, 3714–3719.
23. Xua, Z.; Zhang, H.; Zhong, H.; Lu, Q.; Wang, Y.; Su, D. Effect of Particle Size on the Activity and Durability of the Pt/C Electrocatalyst for Proton Exchange Membrane Fuel Cells. *Appl. Catal., B* **2012**, *111–112*, 264–270.
24. Lim, B.; Jiang, M.; Camargo, P. H. C.; Cho, E. C.; Tao, J.; Lu, X.; Zhu, Y.; Xia, Y. Pd–Pt Bimetallic Nanodendrites with High Activity for Oxygen Reduction. *Science* **2009**, *324*, 1302–1305.
25. Oezaslan, M.; Hasché, F.; Strasser, P. Pt-Based Core–Shell Catalyst Architectures for Oxygen Fuel Cell Electrodes. *J. Phys. Chem. Lett.* **2013**, *4*, 3273–3291.
26. Wang, J. X.; Inada, H.; Wu, L.; Zhu, Y.; Choi, Y.; Liu, P.; Zhou, W.-P.; Adzic, R. R. Oxygen Reduction on Well-Defined Core–Shell Nanocatalysts: Particle Size, Facet, and Pt Shell Thickness Effects. *J. Am. Chem. Soc.* **2009**, *131*, 17298–17302.
27. Xie, S.; Choi, S.-I.; Lu, N.; Roling, L. T.; Herron, J. A.; Zhang, L.; Park, J.; Wang, J.; Kim, M. J.; Xie, Z.; Mavrikakis, M.; Xia, Y. Atomic Layer-by-Layer Deposition of Pt on Pd Nanocubes for Catalysts with Enhanced Activity and Durability toward Oxygen Reduction. *Nano Lett.* **2014**, *14*, 3570–3576.
28. Zhang, J.; Lima, F. H. B.; Shao, M. H.; Sasaki, K.; Wang, J. X.; Hanson, J.; Adzic, R. R. Platinum Monolayer on Non noble Metal–Noble Metal Core–Shell Nanoparticle Electrocatalysts for O_2 Reduction. *J. Phys. Chem. B* **2005**, *109*, 22701–22704.
29. Choi, R.; Choi, S.-I.; Choi, C. H.; Nam, K. M.; Woo, S. I.; Park, J. T.; Han, S. W. Designed Synthesis of Well-Defined Pd@Pt Core–Shell Nanoparticles with Controlled Shell Thickness as Efficient Oxygen Reduction Electrocatalysts. *Chem.—Eur. J.* **2013**, *19*, 8190–8198.
30. Humbert, M. P.; Smith, B. H.; Wang, Q.; Ehrlich, S. N.; Shao, M. Synthesis and Characterization of Palladium–Platinum Core–Shell Electrocatalysts for Oxygen Reduction. *Electrocatalysis* **2012**, *3*, 298–303.
31. Peng, Z. M.; Yang, H. Synthesis and Oxygen-Reduction Electrocatalytic Property of Pt-on-Pd Bimetallic Hetero-nanostructures. *J. Am. Chem. Soc.* **2009**, *131*, 7542–7543.
32. Kitchin, J. R.; Nørskov, J. K.; Barteau, M. A.; Chen, J. G. Role of Strain and Ligand Effects in the Modification of the Electronic and Chemical Properties of Bimetallic Surfaces. *Phys. Rev. Lett.* **2004**, *93*, 156801.
33. Shao, M.; Yu, T.; Odell, J. H.; Jin, M.; Xia, Y. Structural Dependence of Oxygen Reduction Reaction on Palladium Nanocrystals. *Chem. Commun.* **2011**, *47*, 6566–6568.
34. Lim, B.; Wang, J.; Camargo, P. H. C.; Jiang, M.; Kim, M. J.; Xia, Y. Facile Synthesis of Bimetallic Nanoplates Consisting of Pd Cores and Pt Shells through Seeded Epitaxial Growth. *Nano Lett.* **2008**, *8*, 2535–2540.
35. Lee, Y. H.; Lee, G.; Shim, J. H.; Hwang, S.; Kwak, J.; Lee, K.; Song, H.; Park, J. T. Monodisperse PtRu Nanoalloy on Carbon as a High-Performance DMFC Catalyst. *Chem. Mater.* **2006**, *18*, 4209–4211.
36. Mazumder, V.; Sun, S. Oleylamine-Mediated Synthesis of Pd Nanoparticles for Catalytic Formic Acid Oxidation. *J. Am. Chem. Soc.* **2009**, *131*, 4588–4589.
37. Zhang, H.; Jin, M.; Liu, H.; Wang, J.; Kim, M. J.; Yang, D.; Xie, Z.; Liu, J.; Xia, Y. Facile Synthesis of Pd–Pt Alloy Nanocages and Their Enhanced Performance for Preferential Oxidation of CO in Excess Hydrogen. *ACS Nano* **2011**, *5*, 8212–8222.
38. Shao, M. H.; Odell, J. H.; Choi, S.-I.; Xia, Y. Electrochemical Surface Area Measurements of Platinum- and Palladium-Based Nanoparticles. *Electrochem. Commun.* **2013**, *31*, 46–48.
39. Ahmadi, M.; Behafarid, F.; Cui, C.; Strasser, P.; Cuenya, B. R. Long-Range Segregation Phenomena in Shape-Selected Bimetallic Nanoparticles: Chemical State Effects. *ACS Nano* **2013**, *7*, 9195–9204.
40. Cui, C.; Ahmadi, M.; Behafarid, F.; Gan, L.; Neumann, M.; Heggen, M.; Cuenya, B. R.; Strasser, P. Shape-Selected Bimetallic Nanoparticle Electrocatalysts: Evolution of Their Atomic-Scale Structure, Chemical Composition, and Electrochemical Reactivity under Various Chemical Environments. *Faraday Discuss.* **2013**, *162*, 91–112.
41. Sanles-Sobrido, M.; Banobre-Lopez, M.; Salgueirino, V.; Correa-Duarte, M. A.; Rodriguez-Gonzalez, B.; Rivas, J.; Liz-Marzan, L. M. Tailoring the Magnetic Properties of Nickel Nanoshells through Controlled Chemical Growth. *J. Mater. Chem.* **2010**, *20*, 7360–7365.